Lab on a Chip

PAPER

View Article Online
View Journal | View Issue

Cite this: *Lab Chip*, 2024, **24**, 2920

Operando scanning electron microscopy platform for *in situ* imaging of fluid evolution in nanoporous shale†

Artur Davletshin and Wen Song *

Received 12th December 2023,
Accepted 11th April 2024

DOI: 10.1039/d3lc01066j

rsc.li/loc

Fluid–solid interactions in nanoporous materials underlie processes fundamental to natural and engineered processes, including the thermochemical transformation of argillaceous materials during high-level nuclear waste disposal. *Operando* fluid–solid resolution at the nanoscale, however, is still not possible with existing optical and electron microscopy approaches that are constrained by the diffraction limit of light and by vacuum-fluid incompatibility, respectively. In this work, we develop an *operando* scanning electron microscopy (SEM) platform that enables the first direct *in situ* imaging of dynamic fluid–solid interactions in nanoporous materials with spatio-temporal-chemical resolutions of ~2.5 nm per pixel and 10 fps, along with elemental distributions. Using this platform, we reveal necessary conditions for thermochemical pore and fracture generation in shales and measure their surface wetting characteristics that constrain the feasibility of high-level nuclear waste containment. Notably, we show that low heating-rate conditions typical of radioactive decay produce hydrocarbon liquids that wet fracture and pore surfaces in a self-sealing manner to impede aqueous radionuclide advection.

Introduction

The secure disposal of high-level nuclear waste requires repository materials with extraordinary capacities to contain and retain potential leaked radionuclides.[1–3] Argillaceous formations such as the Boom clays in Belgium, for example, comprised primarily of clays (~20 to 60 wt% smectite, illite, and kaolinite), quartz (~20 to 50 wt%), and organic matter (~5 wt%),[4–6] show exceptional potential to immobilize radioactive cations and to self-seal.[6–11] Nanoscale pores in the clay (~1 to 10 nm), favorably, provide ultralow matrix permeability that bars the transport of fluids, including aqueous phases carrying radioactive cations.[1,12–14] Further, charged clay mineral surfaces have a remarkable capacity for cation adsorption (specific surface area ~100 to 1000 $m^2\ g^{-1}$, cation exchange capacity CEC ~10 to 100 meq/100 g) that likewise immobilize aqueous radionuclides.[3,12,15]

Questions remain, however, on the influence of residual heat from high-level waste cooling on the structural and hydrodynamic integrity of the repository.[13,16] Abundant organic matter (*i.e.*, kerogen) introduced by complex depositional environments undergo heat-induced phase and molecular transformations (*i.e.*, thermal decomposition into hydrocarbon fluids)[4,5] and raise two longstanding questions that undermine the storage security of radioactive wastes in argillaceous materials. First, thermochemical pore and microfracture development at the organic–mineral interface is observed commonly post-mortem.[17–19] While frequently dismissed as an artefact of thermal contraction during *ex situ* imaging,[20–23] connective pore and fracture development, if faithful, contribute potential pathways that enable leaked radionuclide advection.[17,19,24,25] Second, hydrocarbons generated during decay heating and their occupancy (*i.e.*, wettability) of newly developed flow paths influence aqueous phase convection by enhancing waste transport along water-wetted surfaces and inhibiting their advection otherwise.[26,27] These longstanding questions on multiphase transport in heat-altered shales remain unanswered in part because of a lack of *operando* resolution at the micro/nanoscopic pore and fracture scales.

Progress in *operando* visualization techniques over recent decades have advanced greatly the characterization and understanding of fluid behavior at micro/nanoscales. Notably, geochemical microfluidics – optical microscopy platforms fabricated or functionalized with geologic minerals that mimic the pore geometry and surface mineralogy of natural geologic materials[28–34] – enable *operando* visualization of complex multiphase, microscale reactive transport processes *in situ*. Fundamental pore-level fluid–rock interactions resolved using geochemical microfluidics, however, are constrained by the diffraction limit of visible

Center for Subsurface Energy and the Environment, University of Texas at Austin, USA. E-mail: wensong@utexas.edu

† Electronic supplementary information (ESI) available. See DOI: https://doi.org/10.1039/d3lc01066j

light (~250 nm) and fail to access nanoscopic processes important in argillaceous media. Environmental SEM (ESEM) operates under reduced vacuum environments to enable fluid visualization[35] by sacrificing resolution, albeit unable to enable *operando* visualization of flow and realistic fluid systems. Powerfully, recent developments in liquid-phase transmission electron microscopy (LP-TEM) have achieved nanoscopic (*i.e.*, <100 nm) dynamic fluid resolution by isolating fluid samples from the TEM vacuum chamber using a parallel pair of electron-transparent membranes.[36–39] While a step forward, the ability to visualize and measure *in situ* nanoscale fluid–solid interactions confined in porous materials such as argillaceous rock remains missing.

Here, we develop a novel *operando* scanning electron microscopy (SEM) platform that enables the first *in situ* imaging of dynamic fluid–rock interactions at the micro/nanoscale to elucidate the impact of thermochemical transformations on waste storage security in argillaceous repositories. Using the novel *operando* SEM platform, we visualize thermogenic microfracture nucleation and propagation in the mineral matrix to elucidate thermal stress conditions necessary for fracture development. Quantitative capabilities of the visual approach are validated by comparing imaging-based rates of organic matter thermolysis with bulk measurements, where compositional heterogeneity between organic solids is elucidated at the microscale for the first time. Notably, the *operando* wettability and organic matter decomposition characterizations developed here inform a set of thermal stress criteria where thermogenic flow paths become self-sealed to promote long-term waste storage security.

Materials and methods

A middle-Devonian shale from Central Ohio was used in this study. The hydrocarbon (HC) composition of the sample, characterized using flame ionization detection (FID, Table S1†), showed that ~2.64 to 2.68 $mg_{HC}\ g_{rock}^{-1}$ was released *via* thermal desorption (S1 peak) whereas pyrolysis generated ~55.8 to 56.9 $mg_{HC}\ g_{rock}^{-1}$ (S2 peak). The total organic content of this sample was 7.9 to 8.0 wt%, consistent with the organic content of the Boom clays. For this sample, the maximum rate of hydrocarbon generation was at a temperature of T_{max} = 434 ± 1 °C, with a hydrogen index (HI) of 707 to 720 and an oxygen index (OI) of 3 to 4. Mineralogy characterization using X-ray diffraction (XRD, Rigaku R-Axis Spider) showed that the sample was comprised primarily of quartz, illite, kaolinite, and smectite (Fig. S4 and Table S2†).

Once collected and characterized, shale samples were cut into 1 × 1 × 1 cm cubes and polished mechanically using a fine suspension with a particle size of 0.06 μm (TedPella). The polished samples were ion-milled (Leica TIC020 Ion Miller) to achieve a smooth surface for imaging. For non-isothermal experiments ($dT/dt > 0$) where fractures were induced, the samples were cut to ~6 mm × 6 mm × 7 mm such that no compressive stresses were applied from the sample well. Here, a pressure relief valve was used to constrain the *in situ* pressure in the platform. For high temperature isothermal experiments ($dT/dt \sim 0$) where kerogen thermolysis occurred, the samples were cut to between ~6.95 mm × 6.95 mm × 7 mm and 6.99 mm × 6.99 mm × 7 mm to provide confining stress during heating. Specifically, we leverage the differential thermal expansion coefficients for stainless steel ($17.2 \times 10^{-6}\ °C^{-1}$) and shale ($\sim 20 \times 10^{-6}\ °C^{-1}$) to confine the shale sample. Here, the average internal stress of the sample was ~50 MPa during high temperature isothermal heating experiments (Fig. S10†). Before each experiment, a thin layer of gold was deposited on the material samples to minimize surface charging during SEM imaging (EMS Sputter Coater).

Fluid–solid interactions were imaged directly in a scanning electron microscope (FEI Quanta 650) with energy dispersive X-ray spectroscopy (EDS) and Everhart–Thornley detection (ETD) by inserting the prepared samples in the stainless steel sample well of the *operando* SEM cell. The material samples were isolated from the SEM vacuum chamber by a SiN_x membrane (Ted Pella). Two types of membranes were used here: a 9-window Si frame where each membrane window is 50 μm × 50 μm × 15 nm, and a Si frame with a single SiN_x membrane window that is 150 μm × 50 μm × 35 nm. To seal the sample inside the *operando* platform, two copper gaskets (thickness ~200 μm) were compressed between the compression cover, membrane, and sample well.

Thermal control at elevated temperatures was enabled by inserting the platform assembly into an outer insulation cell (Fig. S1†). Heating was delivered to the material sample using an 80 W cartridge heater (Insertion heater, McMaster-Carr) that is coupled to two K-type thermocouples (ESI,† Fig. S1 and S3). The thermocouple data were calibrated for vacuum conditions (Fig. S2†). Feedback control between the thermocouples and the heater was enabled using an Arduino nano control breadboard with a MAX6675 chip for thermocouple connection and a 5 V relay (CozParts). The platform assembly was equipped with a Bluetooth chip (Tech HC-5 Bluetooth Serial Pass-through Module, DSD TECH) that enables remote access during imaging to set heating rates, target temperatures, and power applied to the heaters.

Reaction kinetics measured using time-resolved imaging data were compared with thermogravimetric analyses (TGA, Mettler Thermogravimetric Analyzer Model TGA/DSC 1). Powdered shale samples were heated following the schema used in the *operando* SEM experiments. Heating rates from 3 to 10 °C min^{-1} were applied to evaluate the effects of non-isothermal heating. Isothermal experiments were performed at temperatures ranging from 250 °C to 450 °C to establish residual heating loads imposed by nuclear waste decay.

Results and discussion

Operando SEM platform

A novel *operando* platform that allows the first *in situ* SEM imaging of dynamic fluid–solid interactions in nanoporous

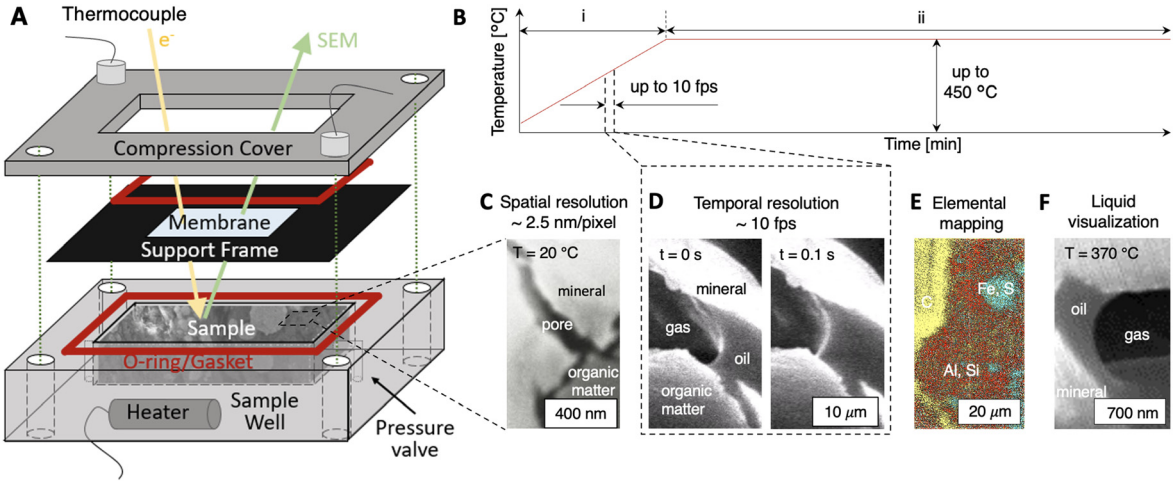

Fig. 1 A novel *operando* scanning electron microscopy (SEM) platform that enables direct *in situ* imaging of dynamic fluid–solid interactions in nanoporous materials. (A) The platform comprises three main components: a sample well where a wet porous sample is emplaced; an electron-transparent membrane to enclose the sample within the platform and to enable electron beam transmission; and a compression cover with O-rings/gaskets to isolate the enclosed porous sample from the SEM chamber vacuum. Experiments at elevated temperatures are enabled by a heater and thermocouple feedback control, and >1 atm pressure is maintained by the membrane and a pressure relief valve. Importantly, the platform is fully self-contained, Bluetooth-controlled, and functions in any SEM experiment without the need for modification or feedthroughs. (B–F) Capabilities of the platform include (B) thermal control up to 450 °C with (i) non-isothermal and (ii) isothermal modulation, (C) *operando* spatial resolutions down to ~2.5 nm per pixel, (D) temporal resolutions up to ~10 fps, (E) spatial elemental mapping using energy dispersive X-ray spectroscopy (EDS), and (F) liquids–gas–solid interfacial imaging at elevated temperatures and pressures.

materials is developed (Fig. 1). The platform marries concepts from geochemical microfluidics and LP-TEM to isolate wetted geologic samples from SEM vacuum environments while enabling direct electron imaging. The function of the platform is enabled by its three main components (Fig. 1A): (i) a sample well (7 mm × 7 mm × 8 mm in depth) that holds the wetted material sample; (ii) an electron-transparent membrane (*e.g.*, silicon nitride, SiN_x) that encloses the sample within the sample well while maintaining electron beam transmission; and (iii) a compression cover with O-rings and/or gaskets that isolates the wetted rock sample (>1 atm) from the SEM vacuum environment (~10^{-7} torr).

Powerfully, the novel platform effectively enables *operando* imaging of dynamic fluid–rock interactions at elevated temperatures (Fig. 1B) with spatial resolutions down to ~2.5 nm per pixel (Fig. 1C) and temporal resolutions up to ~10 fps (Fig. 1D). Spatially-resolved mapping of elemental species is enabled by SEM energy dispersive X-ray spectroscopy (SEM–EDS, Fig. 1E) to inform the progress of thermochemical reactions. For the first time, nanoscale pore-level liquid/gas/solid interfaces can be resolved dynamically *in situ* (Fig. 1F). Fluid pressures are maintained by the SiN_x membrane (Young's modulus ~280 to 290 GPa)[40] and a pressure relief valve. Thermal control up to ~450 °C with non-isothermal (Fig. 1B, i, $dT/dt > 0$) and isothermal modulations (Fig. 1B, ii, $dT/dt \sim 0$) is enabled using a cartridge heater, thermocouple, and PID Bluetooth system (see Materials and methods). Notably, the self-contained platform system operates independently of feedthroughs and is functional in any SEM without modification. The key capabilities of the *operando* platform are demonstrated below in shale, namely, spatio-temporal resolution with *in situ* imaging, quantification of reaction kinetics, and *operando* fluid–solid interactions.

In situ imaging: thermogenic fracture development

We first demonstrate the utility of the *operando* SEM platform by imaging *in situ* thermochemical fracture and pore development in organic-rich shales (Fig. 2 and 3). Here, a shale sample comprised primarily of quartz and clay minerals (Fig. 2A, light gray material) with organic matter fragments (Fig. 2A, dark gray material) is imaged during heating up to ~450 °C. The organic solids in this sample comprise short-chain molecules that vaporize into hydrocarbon gases at low temperatures ($T < 300$ °C, Fig. 2B, C, II, blue shaded region) and heavy components that thermolyze into hydrocarbon fluids at elevated temperatures (*i.e.*, $T > 300$ °C, Fig. 2B, C, III, yellow shaded region). Capillarity-bound water is vaporized at temperatures below ~120 °C (Fig. 2B, C, I, pink shaded region).

During non-isothermal heating ($dT/dt \sim 3$, 7.5 °C min^{-1}), microfractures begin to nucleate and propagate at temperatures of ~120 °C (Fig. 2). Comparison with thermogravimetric analyses (TGA) show that fracture generation occurs during the vaporization of light hydrocarbons (Fig. 2B, C, region II, $T > 120$ °C) rather than that of capillarity-bound water (Fig. 2B, C, region I, $T < 120$ °C). We note, however, that water vaporization may contribute to local pressure buildup and ultimately matrix fracturing, although the samples here held no significant pore water initially (~1 wt%).

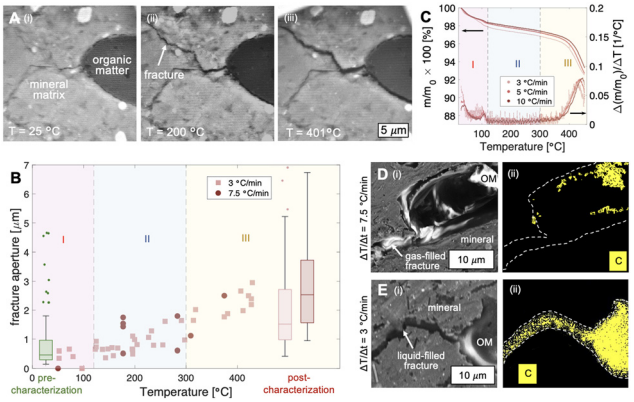

Fig. 2 *In situ* characterization of heat-induced fracturing in organic-rich argillaceous sediments using the *operando* platform. (A) A shale sample (i) comprised primarily of quartz and clay minerals (light gray material) with an initially intact piece of organic matter (dark gray material, OM) is subjected to heating. (ii and iii) During non-isothermal heating (*i.e.*, dT/dt > 0), microfractures nucleate at curved organic/inorganic material interfaces and propagate into the mineral matrix. (B) *In situ* fracture aperture characterization with temperature shows that fracturing initiates at ~120 °C. During non-isothermal heating, apertures open with increasing temperature and heating rate (*e.g.*, dT/dt = 7.5 and 3 °C min^{-1}). (C) Correlation with thermogravimetric analyses show that microfracture nucleation and propagation are controlled by the vaporization of light and heavy hydrocarbon components (regimes II and III, respectively, blue- and yellow-shaded regions). Here, hydrocarbon vapors trapped by the surrounding low permeability mineral matrix (~nD) are unable to evacuate its source pore space and results in local pressure buildup, stress concentration, and stress failure at the tips of the lens-shaped OM. Vapors arising from moisture content are secondary here, with minimal fracturing observed for temperatures < 120 °C (regime I, pink shaded region). (D and E) Multiphase transport characteristics of the fractured shale is controlled by the heating rate. High thermal stress (D, dT/dt = 7.5 °C min^{-1}) results in gas-saturated fractures that allow water imbibition (lack of carbon in EDS map generated fracture, Dii), whereas fractures generated during slow heating (E, dT/dt = 3 °C min^{-1}) are saturated with hydrocarbon liquids (EDS map of carbon occupying fractures, Eii) that impede water transport.

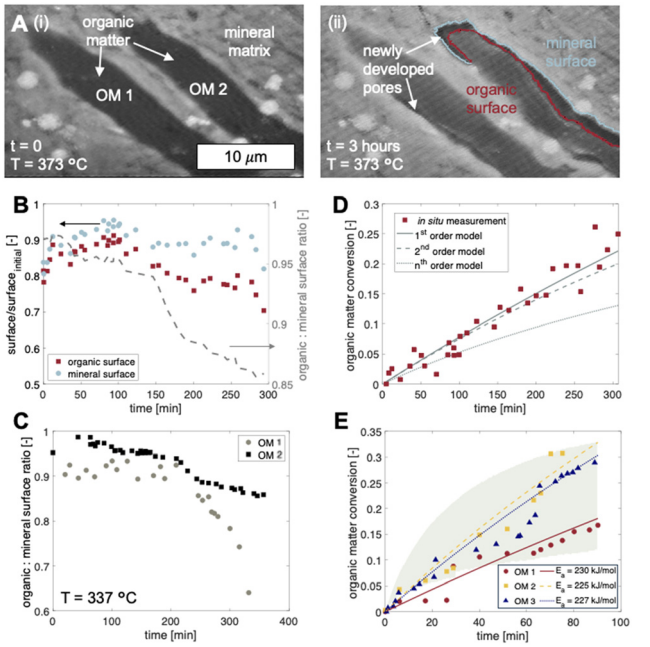

Fig. 3 Pore development in organic-rich shale due to solid organic matter decomposition during high temperature heating (T > 300 °C). (A) A shale sample (i) with two organic matter fragments (OM 1 and OM 2) is heated at temperatures exceeding the pyrolysis threshold (T = 373 °C > 300 °C). (ii) Thermal decomposition of the organic solids is observed after 3 hours of isothermal heating. Here, new organic– and mineral–fluid interfaces are created. Interestingly, two organic fragments in close proximity to one another (OM 1 and OM 2) experience differential rates of thermal decomposition in the same experiment. (B) Fluid–solid interface evolution of a single kerogen fragment shows that decomposition initiates at the mineral–organic interface. Whereas the mineral surface generated is relatively constant over time, organic surfaces diminish with reaction because of decreasing OM volumes. (C) Microscale compositional heterogeneity between adjacent organic fragments lead to differential rates of organic surface generation. (D) Quantification of *in situ* imaging data are consistent with bulk analytical measurements and show that thermal decomposition for individual organic fragments is described by a first order reaction model with Arrhenius kinetics. (E) Differential rates of thermal decomposition between adjacent organic fragments during the same experiment have different activation energies, E_a and hence different chemical compositions. Thermolysis rates for individual organic fragments at 373 °C (data points) are consistent with bulk TGA characterizations between 350 and 400 °C (green shaded region).

In all cases observed in this work, the microfractures nucleate at the curved organic/mineral interface and propagate into the mineral matrix (Fig. 2A). This pattern of fracture nucleation and propagation suggests stress concentration at the organic/mineral interface. We note here that light hydrocarbon vapors are generated at a rate that exceeds its ability to diffuse into the surrounding silicate matrix (permeability ~nD) during rapid heating (*e.g.*, dT/dt ~ 3 and 7.5 °C min^{-1}). As a result, hydrocarbon vapors are instead trapped and pressurize its parent organic structure. The resulting stress is concentrated at the curved tips of the organic/mineral interface where failure and fracturing initiate.

In the context of waste containment, microfracture propagation into the mineral matrix provides a set of high permeability pathways for fluid transport. The presence of generated hydrocarbon fluids (gases and liquids) within the microfractures, however, influence significantly the advective leakage potential of aqueous radionuclides. For fast heating rates (*e.g.*, dT/dt = 7.5 °C min^{-1}) where heat conduction through the organic fragment is slow compared to the heat influx from the continuous mineral matrix, hydrocarbon vapors are generated and result in gas-saturated fractures that allow water imbibition. Conversely, the fractures generated during low-rate heating (*e.g.*, dT/dt = 3.5 °C min^{-1}) are saturated with hydrocarbon liquids that potentially impede water convection. These complex multiphase fluid dynamics are important considerations in the selection of sites appropriate for nuclear waste disposal.

Reaction kinetics quantification: organic matter thermolysis

For temperatures exceeding the thermolysis threshold of the organic solids in the sample (T > ~300 °C), isothermal

heating leads to pore development at the organic–mineral interface (Fig. 3). Here, a shale sample with organic matter fragments (Fig. 3A, i) is subjected to heating at 373 °C for 3 hours. Time-resolved image sequences show that thermolytic pore creation begins at the organic–mineral interface (Fig. 3A, ii) and propagates into the organic solid. Specifically, thermogenic pores begin as thin gaps between organic and mineral phases with organic-to-mineral surface ratios close to unity (Fig. 3B, C, t = 0 to 100 min). Sustained organic solid thermolysis at elevated temperatures leads to the inward development of pores (*i.e.*, into the organic solid) and decreasing organic-to-mineral surface ratios (Fig. 3B, C, $t > 100$ min). Evolving ratios of organic and mineral surfaces here, each described by distinct wetting and sorption characteristics, contribute potential changes to the multiphase transport (*e.g.*, relative permeability) of aqueous radionuclides. Compositional heterogeneities between organic fragments, interestingly, give rise to differential rates of organic surface generation (Fig. 3C).

Quantitative capabilities of the *operando* visualization platform are demonstrated by comparing *in situ* image sequences of micro/nanoscopic organic fragment thermolysis to bulk characterizations. As in bulk pyrolysis measurements, quantification of *in situ* imaging shows that the thermolytic reaction rates for individual organic fragments are best described using a first-order reaction model (Fig. 3D, Table S3†):

$$\frac{\mathrm{d}[\mathrm{OM}]}{\mathrm{d}t} = -k[\mathrm{OM}]^n,$$

where the decomposition rate of organic matter, OM, decays exponentially over time as n = 1. Here, the kinetics, k, are described by the Arrhenius equation:

$$k = A\mathrm{e}^{-E_\mathrm{a}/RT},$$

where the pre-exponential factor A = 1.5 × 10^{14} s^{-1} and activation energy E_a = 230 kJ mol^{-1} are taken from bulk characterization reported in the literature.[41,42] The temperature is T = 373 °C and corresponds to the *in situ* experimental conditions. Despite identical thermal stressing (*i.e.*, from the same experiment), we note that organic fragments adjacent to one another experience differential rates of thermal decomposition (Fig. 3A and E). These fragment-specific differences are captured by distinct activation energies, E_a (Fig. 3E, $E_{\mathrm{a},1}$ = 230 kJ mol^{-1}, $E_{\mathrm{a},2}$ = 225 kJ mol^{-1}, and $E_{\mathrm{a},3}$ = 227 kJ mol^{-1}) that may reflect heterogeneities in molecular composition (Fig. 3E, lines). For each organic fragment, the imaging-based rates of thermolysis at 373 °C (Fig. 3E, data points) and first-order reaction models (Fig. 3E, lines) are consistent with bulk reaction rates measured using TGA for temperatures between 350 °C and 400 °C (Fig. 3E, green shaded region).

We note here that the fractures and pores observed at organic–mineral interfaces are not a result of thermal contraction as postulated in previous investigations. Whereas inconclusive results in the literature stem from the experimental uncertainties of *ex situ* characterization,[20–22,24,25,43,44] our *operando* experiments prove conclusively that at relatively high rates of heating (*e.g.*, those encountered during decay heating), fractures and pores develop *via* microscale organic matter decomposition at the organic–mineral interface (Movie S1†). In other words, the pores developed here are a result of phase and molecular transformations of the organic solids rather than thermomechanical coupling. Importantly, morphologies observed here provide new insight into the connectivity and fluid transmissibility of thermogenic flow paths that potentially undermine waste storage security.

In situ wetting characterization

Surface wetting characteristics of thermogenic pores and fractures determine the advection of leaked radionuclides in the aqueous phase. Here, we provide the first *in situ* nanoscale resolution of dynamic fluid–solid interactions in a porous material (Fig. 4 and Movie S2†). Specifically, hydrocarbon liquids and gases generated during organic solid thermolysis (heating from 25 to 370 °C) are imaged in a shale sample (Fig. 4A). Fluid distributions are characterized *in situ* to elucidate their pore-occupancy tendencies (*i.e.*,

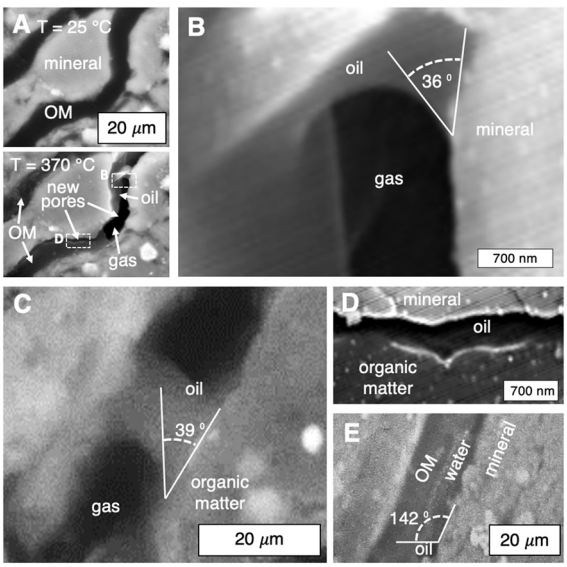

Fig. 4 *In situ* nanoscale fluid–solid interactions are visualized for the first time. (A) A shale sample subjected to thermal stress is heated from 25 to 370 °C. Organic matter decomposition is observed, including the generation of hydrocarbon liquids and gases in the newly created pore space. (B–E) Contact angle characterization *in situ* shows that the newly generated pore surfaces are oil-wet. Oil wets the (B) mineral and (C) organic surfaces in the presence of gas. (D) Pores generated from kerogen decomposition between mineral and organic solids are imbibed spontaneously with hydrocarbon liquids. Oil-saturated flow paths impede the transport of radionuclide-contaminated aqueous phases. (E) Water is non-wetting in pore spaces between organic and mineral solids in the presence of hydrocarbon liquids.

wettability) and their influence on water transport (Fig. 4B to E).

Operando contact angle measurements at 370 °C show that the mineral (Fig. 4B) and organic (Fig. 4C) surfaces of the thermogenic flow paths are oil–wet in the presence of gas. Recall that for heating rates representative of decay heat, hydrocarbon liquids are generated (Fig. 2E) rather than gases (Fig. 2D). It is therefore possible that, during organics thermolysis, hydrocarbon liquids (*i.e.*, oils) imbibe spontaneously into and saturate the newly generated flow paths (Fig. 4D). Importantly, we note that water is non-wetting here (Fig. 4E), and subsequent convection of radionuclide-bearing water through pores and fractures is impeded by the wetting oil phase. In other words, the thermogenic pores and fractures are self-sealed by the wetting hydrocarbon liquids. Together, the wetting characteristics of mineral and organic surfaces constrain a set of heating rates (*i.e.*, waste density) that enable fractures to self-seal and provides an additional mechanism to contain possible leaked radionuclides.

Conclusions

The *operando* SEM imaging platform developed here provides a first-of-its-kind spatio-temporal-chemical resolution of dynamic fluid–solid interactions in porous materials that underlie a breadth of natural and engineered processes, including longstanding uncertainties surrounding thermogenic pore and fracture development at organic–mineral interfaces in shale. The *operando* resolutions of ~2.5 nm per pixel and ~10 fps achieved here enable reasonable quantification of micro/nanoscale reaction rates that are consistent with bulk measurements. Microscale heterogeneities are captured for the first time, and *in situ* fluid distributions in the generated flow paths provide insight into the self-sealing potential of argillaceous materials that ensure the long-term security of radioactive waste storage.

Conflicts of interest

There are no conflicts to declare.

Acknowledgements

The authors acknowledge funding in part from the American Chemical Society grant PRF 61218-DNI9 and NSF grant CBET-2145374.

Notes and references

1 C. D. Hollister, D. R. Anderson and G. R. Heath, Subseabed disposal of nuclear wastes, *Science*, 1979, **1981**(213), 4514.
2 G. De Marsily, E. Ledoux, A. Barbreau and J. Margat, Nuclear Waste Disposal: Can the Geologist Guarantee Isolation?, *Science*, 1979, **1977**(197), 4303, Available from: **https://www.science.org**.
3 S. E. Bone, J. J. Dynes, J. Cliff and J. R. Bargar, Uranium(IV) adsorption by natural organic matter in anoxic sediments, *Proc. Natl. Acad. Sci. U. S. A.*, 2017, **114**(4), 711–716.
4 C. Tournassat, A. Vinsot, E. C. Gaucher and S. Altmann, Chemical Conditions in Clay-Rocks, in *Developments in Clay Science*, Elsevier, 2015, pp. 71–100.
5 Y. F. Deng, Y. J. Cui, A. M. Tang, X. L. Li and X. Sillen, An experimental study on the secondary deformation of Boom clay, *Appl. Clay Sci.*, 2012, **59–60**, 19–25.
6 L. Frederickx, M. Honty, M. De Craen, R. Dohrmann and J. A. N. Elsen, Relating the cation exchange properties of the boom clay (Belgium) to mineralogy and pore-water chemistry, *Clays Clay Miner.*, 2018, **66**(5), 449–465.
7 C. E. Neuzil, Can shale safely host U.S. nuclear waste?, *Eos*, 2013, **94**(30), 261–262.
8 X. Liu, C. Tournassat, S. Grangeon, A. G. Kalinichev, Y. Takahashi and M. M. Fernandes, Molecular-level understanding of metal ion retention in clay-rich materials, *Nat. Rev. Earth Environ.*, 2022, **3**, 461–476.
9 B. Helmut, D. Boris, D. C. Martin, A. de Haller, M. Martin and F. Skoczylas, *et al.* Self-sealing of fractures in argillaqceous formations in the context of geological disposal of radioactive waste: review and synthesis, OECD, 2010.
10 L. Ortiz, G. Volckaert and D. Mallants, Gas generation and migration in Boom Clay, a potential host rock formation for nuclear waste storage, *Eng. Geol.*, 2002, 287–296, Available from: **https://www.elsevier.com/locate/enggeo**.
11 D. G. Brookins, Shale as a repository for radioactive waste: the evidence from Oklo, *Environ. Geol.*, 1976, **1**, 255–259.
12 W. M. Alley and R. Alley, The growing problem of stranded used nuclear fuel, *Environ. Sci. Technol.*, 2014, **48**(4), 2091–2096.
13 Y. Wang, D. L. Porter, S. E. Naleway and P. Newell, Thermo-mechanical characterization of shale using nanoindentation, *Sci. Rep.*, 2021, **11**(1), 18864.
14 B. Marty, S. Dewonck and C. France-Lanord, Geochemical evidence for efficient aquifer isolation over geological timeframes, *Nature*, 2003, **425**(6953), 55–58.
15 F. Macht, K. Eusterhues, G. J. Pronk and K. U. Totsche, Specific surface area of clay minerals: Comparison between atomic force microscopy measurements and bulk-gas (N2) and -liquid (EGME) adsorption methods, *Appl. Clay Sci.*, 2011, **53**(1), 20–26.
16 J. Berthonneau, A. Obliger, P. L. Valdenaire, O. Grauby, D. Ferry and D. Chaudanson, *et al.* Mesoscale structure, mechanics, and transport properties of source rocks' organic pore networks, *Proc. Natl. Acad. Sci. U. S. A.*, 2018, **115**(49), 12365–12370.
17 Y. Kang, Z. Hao, Q. Chen, L. You, M. Chen and J. Tian, *et al.* Heating-Induced Enhancement of Shale Gas Transport and Its Application for Improving Hydraulic Fracturing Performance, *Energy Fuels*, 2022, **36**(24), 14682–14695.
18 S. P. Rigby, H. Jahan, L. Stevens, C. Uguna, C. Snape and B. Macnaughton, *et al.* Pore structural evolution of shale

following thermochemical treatment, *Mar. Pet. Geol.*, 2020, **112**, 104058.

19 T. W. Kim, C. M. Ross, K. M. Guan, A. K. Burnham and A. R. Kovscek, Permeability and porosity evolution of organic-rich shales from the Green River formation as a result of maturation, *SPE J.*, 2020, **25**(3), 1377–1405.

20 L. T. Ko, S. C. Ruppel, R. G. Loucks, P. C. Hackley, T. Zhang and D. Shao, Pore-types and pore-network evolution in Upper Devonian-Lower Mississippian Woodford and Mississippian Barnett mudstones: Insights from laboratory thermal maturation and organic petrology, *Int. J. Coal Geol.*, 2018, **190**, 3–28.

21 J. Klaver, G. Desbois, R. Littke and J. L. Urai, BIB-SEM pore characterization of mature and post mature Posidonia Shale samples from the Hils area, Germany, *Int. J. Coal Geol.*, 2016, **158**, 78–89.

22 M. Mastalerz, L. Wei, A. Drobniak, A. Schimmelmann and J. Schieber, Responses of specific surface area and micro- and mesopore characteristics of shale and coal to heating at elevated hydrostatic and lithostatic pressures, *Int. J. Coal Geol.*, 2018, **197**, 20–30.

23 L. T. Ko, R. G. Loucks, T. Zhang, S. C. Ruppel and D. Shao, Pore and pore network evolution of Upper Cretaceous Boquillas (Eagle Ford-equivalent) mudrocks: Results from gold tube pyrolysis experiments, *Am. Assoc. Pet. Geol. Bull.*, 2016, **100**(11), 1693–1722.

24 K. Suwannasri, T. Vanorio and A. Clark, Monitoring the changes in the microstructure and the elastic and transport properties of Eagle Ford marl during maturation, *Geophysics*, 2018, **83**(5), MR263–MR281.

25 A. M. Allan, T. Vanorio and J. E. P. Dahl, Pyrolysis-induced P-wave velocity anisotropy in organic-rich shales, *Geophysics*, 2013, **79**(2), D41–D53.

26 K. Falk, B. Coasne, R. Pellenq, F. J. Ulm and L. Bocquet, Subcontinuum mass transport of condensed hydrocarbons in nanoporous media, *Nat. Commun.*, 2015, **6**, 6949.

27 T. Lee, L. Bocquet and B. Coasne, Activated desorption at heterogeneous interfaces and long-time kinetics of hydrocarbon recovery from nanoporous media, *Nat. Commun.*, 2016, **7**, 11890.

28 W. Song, T. W. De Haas, H. Fadaei and D. Sinton, Chip-off-the-old-rock: The study of reservoir-relevant geological processes with real-rock micromodels, *Lab Chip*, 2014, **14**(22), 4382–4390.

29 A. L. Harrison, G. M. Dipple, W. Song, I. M. Power, K. U. Mayer and A. Beinlich, *et al.* Changes in mineral reactivity driven by pore fluid mobility in partially wetted porous media, *Chem. Geol.*, 2017, **463**(January), 1–11, DOI: **10.1016/j.chemgeo.2017.05.003**.

30 W. Song and A. R. Kovscek, Functionalization of micromodels with kaolinite for investigation of low salinity oil-recovery processes, *Lab Chip*, 2015, **15**, 3314–3325, Available from: **https://xlink.rsc.org/?DOI=C5LC00544B**.

31 W. Song, F. Ogunbanwo, M. Steinsbø, M. A. Fernø and A. R. Kovscek, Mechanisms of multiphase reactive flow using biogenically calcite-functionalized micromodels, *Lab Chip*, 2018, **18**, 3881–3891.

32 M. L. Porter, J. Jiménez-Martínez, R. Martinez, Q. McCulloch, J. W. Carey and H. S. Viswanathan, Geo-material microfluidics at reservoir conditions for subsurface energy resource applications, *Lab Chip*, 2015, **15**, 4044–4053, Available from: **https://pubs.rsc.org/en/content/articlehtml/2015/lc/c5lc00704f**.

33 A. Gerami, P. Mostaghimi, R. T. Armstrong, A. Zamani and M. E. Warkiani, A microfluidic framework for studying relative permeability in coal, *Int. J. Coal Geol.*, 2016, **159**, 183–193, DOI: **10.1016/j.coal.2016.04.002**.

34 B. Ling, M. Sodwatana, A. Kohli, C. M. Ross, A. Jew and A. R. Kovscek, *et al.* Probing multiscale dissolution dynamics in natural rocks through microfluidics and compositional analysis, *Proc. Natl. Acad. Sci. U. S. A.*, 2022, **119**(32), e2122520119.

35 H. J. Deglint, C. R. Clarkson, C. DeBuhr and A. Ghanizadeh, Live Imaging of Micro-Wettability Experiments Performed for Low-Permeability Oil Reservoirs, *Sci. Rep.*, 2017, **7**(1), 4347.

36 F. M. Ross, *Liquid Cell Electron Microscopy*, Cambridge University Press, 2016.

37 N. De Jonge and F. M. Ross, Electron microscopy of specimens in liquid, *Nat. Nanotechnol.*, 2011, **6**, 695–704.

38 L. Liu, J. Chun, X. Zhang, M. Sassi, A. G. Stack and C. I. Pearce, *et al.* Radiolysis and Radiation-Driven Dynamics of Boehmite Dissolution Observed by in Situ Liquid-Phase TEM, *Environ. Sci. Technol.*, 2022, **56**(8), 5029–5036.

39 F. M. Ross, Opportunities and challenges in liquid cell electron microscopy, *Science*, 2015, **350**, 6267.

40 A. Khan, J. Philip and P. Hess, Young's modulus of silicon nitride used in scanning force microscope cantilevers, *J. Appl. Phys.*, 2004, **95**(4), 1667–1672.

41 A. S. Pepper and P. J. Corvit, Simple kinetic models of petroleum formation. Part I: oil and gas generation from kerogen, *Mar. Pet. Geol.*, 1995, **12**(3), 291–319.

42 R. L. Braun and A. K. Burnham, Analysis of chemical reaction kinetics using a distribution of activation energies and simpler models, *Energy Fuels*, 1987, **1**(2), 153–161.

43 L. T. Ko, R. G. Loucks, T. Zhang, S. C. Ruppel and D. Shao, Pore and pore network evolution of Upper Cretaceous Boquillas (Eagle Ford-equivalent) mudrocks: Results from gold tube pyrolysis experiments, *AAPG Bull.*, 2016, **100**(11), 1693–1722.

44 O. H. Ardakani, H. Sanei, A. Ghanizadeh, D. Lavoie, Z. Chen and C. R. Clarkson, Do all fractions of organic matter contribute equally in shale porosity? A case study from Upper Ordovician Utica Shale, southern Quebec, Canada, *Mar. Pet. Geol.*, 2018, **92**, 794–808.